Coastal Engineering 47 (2003) 265–293

Coastal Engineering
An International Journal for Coastal, Harbour and Offshore Engineers

www.elsevier.com/locate/coastaleng

An approach to determining nearshore bathymetry using remotely sensed ocean surface dynamics

Shubhra K. Misra[a,*], Andrew B. Kennedy[b], James T. Kirby[a]

[a] *Ocean Engineering Laboratory, Center for Applied Coastal Research, University of Delaware, Newark, DE 19716, USA*
[b] *Department of Civil and Coastal Engineering, University of Florida, Gainesville, FL 32607, USA*

Received 28 March 2001; received in revised form 31 July 2002; accepted 23 August 2002

Abstract

This paper describes a spatially one-dimensional algorithm developed to estimate water depths from remotely sensed information of the water surface, using extended Boussinesq equations. Local phase speed estimates are obtained using a least-squares approach, from spatial profiles of surface elevation/orbital velocity lagged in time. Inversion algorithms have been developed for both linearized and fully nonlinear Boussinesq equations to calculate the depth. In all cases, synthetic input data are generated using a fully nonlinear time-dependent Boussinesq model. Wave conditions including monochromatic and irregular waves are simulated in the model. Mean flow effects are included in the inversion algorithm to account for currents. For monochromatic wave conditions, there is good agreement between the actual and estimated depth and particle kinematics. The fully nonlinear method, as compared to the linearized inversion, improves the depth prediction by 10% for the test case considered. Irregular wave conditions were simulated using time series generated for a TMA spectrum with varying values of the peak enhancement factor. The error in the inverted depths increased in the deeper part of the bathymetry as the wave train become more broad-banded. For monochromatic waves in the presence of weak currents, the modified algorithm (including mean flow effects) is seen to improve the inverted depth by 10%, over the original formulation.

Keywords: Depth inversion; Boussinesq equations; Ocean waves; Phase speed

1. Introduction

In the dynamically active nearshore region of an ocean, the bed topography changes due to an active interaction between sediment transport and hydrodynamic processes. An accurate knowledge of the ocean floor, particularly in the nearshore region and over various spatial and temporal scales, is very important in understanding such an interactive regime. Traditional surveying methods of quantifying the depth are inherently labor intensive as they involve manual deployment of expensive instruments over the area of interest. Even with sophisticated and accurate depth measuring devices like sonar altimeters and global positioning satellite units, the surveying process remains costly in terms of both time and money. It is not feasible to use these methods to cover large spatial distances. Wave breaking and

* Corresponding author.
E-mail address: shubhra@coastal.udel.edu (S.K. Misra).

0378-3839/02/$ - see front matter
PII: S0378-3839(02)00118-7

strong currents near the shore make in situ measurements of the bathymetry a hazardous task. Moreover, marine fouling, water turbidity and suspended sediments limit the operation times of such instruments. Since there already exists quite a significant amount of understanding of the hydrodynamic coupling between the water depth and the wave kinematics, methods which would determine the ocean bathymetry from remotely measured surface information are likely candidates for further development. With the progressively increasing accuracy and availability of remotely sensed ocean surface information, depth inversion, as it is commonly referred to in literature, has become one of the most promising tools in this area of research.

Depth inversion methods can broadly be classified into two approaches: time domain inversion and frequency domain inversion. Depth inversion in the frequency domain essentially utilizes time stacks of surface information to calculate wave parameters such as the wave frequency, wave number and/or wave celerity, which are then used in the dispersion relationship to invert the depth. Stockdon and Holman (2000) inverted depth based on field data, using digital video images at field sites. Time stacks of pixel intensities at various cross-shore and long-shore arrays were stored. Using Fourier analysis of the data, the long-shore and cross-shore wave number components and the peak frequency were obtained. The linear dispersion relationship

$$C^2 = \frac{g}{k}\tanh(kh) \qquad (1)$$

was then used to invert depth. Here, C is the wave celerity, k is the wave number k=($2\pi/L$), L the wavelength, h is the local water depth and g the acceleration due to gravity. Depths were significantly over-predicted in shallow water and under-predicted in deep water. The analysis of the video signal neglected the effects of surface drift currents, frequency and amplitude dispersion effects, the undertow and rip currents. Broad-banded and directionally spread spectrums degraded the accuracy of the inverted depth estimates, since their effects could not be included. A similar analysis has been used by Holland (2001) for time series data from bottom mounted pressure sensors. He found that the inclusion of finite amplitude effects in the linear dispersion relationship improved his depth predictions. Dugan et al. (1996) have used airborne imaging systems to collect sequential ocean surface maps, and, using 3-D frequency-wave number spectra and the linear dispersion relation, have inverted depth. Bell (1999) has demonstrated the usefulness of a sequence of marine X-band radar images to invert shallow water bathymetry. The inversion algorithm he used is essentially the linear dispersion relationship, with the phase speed and the wave period estimated from cross-correlation and frequency spectra analysis, respectively.

Time domain inversion denotes methods to determine the bathymetry when the surface information is sparse in time. Dalrymple et al. (1998) describe a method using Hilbert transforms to estimate phase speeds from numerically generated surface maps of wave elevation. Gradients of the phase structure were then calculated to determine the wave number. A big disadvantage of this method was the assumption that wave period be known accurately. For spectral sea states, another method was developed using lag-correlation techniques. Auto-correlation and cross-correlation matrices were calculated from the images, and estimates of wavelength and phase speed were respectively obtained. Over-predictions of depth were observed, which were attributed to nonlinearity and/or window size effects on correlation estimates.

Grilli (1998) devised two depth inversion algorithms (DIAs) to include amplitude and frequency dispersion effects in shallow water, when estimating depth from remotely sensed data. His computations were done on a fully nonlinear model based on potential flow theory and the boundary element method. Shoaling periodic regular waves on monotonic and mildly sloping beach profiles were investigated and their properties used to invert depth. Bars and troughs however, are a common feature of interest close to the shoreline and this method cannot account for such changes in topography. His test cases were done with periodic waves, where it was possible to geometrically determine the wave period. This would prove to be difficult for the case of irregular waves, in which several frequencies would be represented in one waveform, as is the case in the real sea state. The marked improvements over depth (three to seven times) over linear inversion predictions, however, demonstrate that any approach to depth inversion should include the complex nonlinear dynamics of wave propagation. Kennedy et al. (2000b) have used a fully nonlinear, time-dependent Boussinesq model as a tool for spatial inversion. The model contains the fully nonlinear extended Boussinesq equations developed by Wei et al. (1995), and further modified by Kennedy et al. (2000a) and Chen et al. (2000) to include the effects of wave breaking, run-up and wave-induced current effects. They assume that time-lagged synthetic spatial maps of both the surface wave height and orbital velocities are available. Overall, depths were predicted accurately. Performing the fully time-dependent Boussinesq inversion was burdensome in terms of computational time.

In the context of time domain depth inversion algorithms, as compared to Kennedy et al. (2000b), we assume a less optimal case of data availability, where information about only one of the two kinematic variables is required for inversion in one horizontal dimension. This is more realistic with reference to the wave information output from existing remote sensing instrumentation platforms. Recently, Hessner et al. (1999b) have discussed the use of space–time behavior of the sea surface elevation (with an accuracy of 10% in the significant wave heights) obtained from nautical radars in estimating the water depth. Reichert et al. (1999) and Hessner et al. (1999a) have compared sea state measurements obtained from a shallow water installation of a remote sensing system based on a nautical X-band radar, to Waverider buoy data, and found that surface current velocities could be estimated to within an accuracy of ± 0.2 m/s. Williams et al. (2000) have reported the application of airborne optical measurements in determining surface current vectors in the nearshore region, accurate to 5% in magnitude and 5E in direction, when compared to ADCP measurements. A time-lagged pair of spatial profiles of wave height and surface velocities obtained from such data acquisition systems can be used to quantify the spatial variability in the phase speeds of propagating water waves as they approach the shoreline. A least-squares based method to estimate local phase speeds is discussed in Section 2.1. In Sections 2.2 and 2.3, we formulate the hydrodynamic equations that relate the given input data and the calculated phase speeds to the unknown bathymetry. The numerical implementation of the inversion algorithm is explained and tested with a simple example in Section 3. Several test cases under varying input wave conditions are shown and the results discussed in Section 4, followed by the conclusions in Section 5.

2. Mathematical formulation

2.1. Phase speed estimation

For spatially dense profiles of ocean surface elevation or velocities separated in time (usually a fraction of a wave period), correlation formulas can be used to calculate local phase speeds over the entire domain. The data are typically analyzed by subdividing the entire domain using finite windows. The waveform is assumed to be locally constant. This essentially implies that the first profile can be translated to the second profile at a later time by the computed phase speed within the window. The window is shifted over the domain in small spatial shifts to get local estimates of the phase speed (Appendix A). However, it can be shown that even for two perfectly sinusoidal signals, the optimal window size is dependent upon the wavelength, the time-lag between the two signals and the time period of the wave (Appendix A.1). The wavelength and the wave period are not known a priori. Real surface data also will never contain purely monochromatic waves, and thus no unique period or length of the wave train can be determined. To avoid the pitfalls mentioned in the previous method, a least-squares based method was developed to calculate local phase speeds from two time-lagged one-dimensional profiles of the surface. For a typical window size on the order of the wavelength, the phase speed estimates are smaller by two orders of magnitude when compared to the cross-correlation estimate (Appendix A.2). Instead of surface elevation data, particle velocity profiles can similarly be used to get local phase speed estimates.

2.2. Linearized shallow water equations

After calculating the local phase speeds throughout the spatial domain, we need to formulate a time-independent set of hydrodynamic equations that relate the given surface data and the computed phase speed to the unknown depth. Since we are trying to estimate the depth in the shallower nearshore part of the ocean, we consider at first the relatively simpler linearized shallow water equations. In one horizontal dimension, the mass equation is

$$\frac{\partial\eta}{\partial t}+\frac{\partial(hu)}{\partial x}=0 \tag{2}$$

The momentum equation is

$$\frac{\partial u}{\partial t}+g\frac{\partial\eta}{\partial x}=0 \tag{3}$$

Assuming a periodic progressive wave traveling in the positive x direction with the form $\eta=a\cos(kx-\omega t)$, we get

$$\frac{\partial\eta}{\partial t}=\omega a\sin(kx-wt)=-\frac{\omega}{k}\frac{\partial\eta}{\partial x}=-C\frac{\partial\eta}{\partial x} \tag{4}$$

The wave number k and the frequency ω are implicitly assumed to be independent of space (x) and time (t), respectively. We can replace the time derivatives with the spatial derivatives and arrive at the shallow water depth inversion mass and momentum equations

$$-C\frac{\partial\eta}{\partial x}+\frac{\partial(hu)}{\partial x}=0 \tag{5}$$

$$-C\frac{\partial u}{\partial x}+g\frac{\partial\eta}{\partial x}=0 \tag{6}$$

If we now integrate along x (assuming that C is locally constant, i.e. $(\partial C/\partial x)=0$), we get,

$$-C\eta+hu=A \tag{7}$$

$$-Cu+g\eta=B \tag{8}$$

where A and B are arbitrary integration constants. If we consider pure wave propagation without mean flow effects, then $A=B=0$, since motion vanishes in the absence of a wave. The case of nonzero values of the constants are discussed later in Section 2.4, where depth-uniform steady currents will be included in the inversion algorithm. Given a time-lagged pair of profiles of η (or u), from which we can calculate C, we can solve Eqs. (7) and (8) for the two unknowns, the depth (h) and the particle velocity u (or η). The shallow water equations, though simple to formulate, are limited by their range of applicability to regions near the shore where the dispersion parameter ($\mu=kh$) is less than about ($\pi/10$). The Boussinesq equations on the other hand, which reduce to the shallow water equations for small values of μ, have been extended to be applicable in regions with values of μ as large as 6, the deep water limit being $\mu>\pi$.

2.3. Boussinesq equations

The extended Boussinesq equations of Wei et al. (1995) have been modified by Chen et al. (2000) and Kennedy et al. (2000a) to include wave breaking, run-up and wave-induced currents and can accurately model wave transformation in the nearshore region. The one-dimensional model equations are

$$\eta_t=E(\eta,u)+vE_2(\eta,u)+f(x,t) \tag{9}$$

$$[U(u)]_t=F(\eta,u)+v[F_2(\eta,u)+F^t(\eta,u_t)]+F_{\mathrm{br}}+F_{\mathrm{b}}+F_{\mathrm{sp}} \tag{10}$$

where $\eta(x,t)$ is the surface elevation and $u(x,t)$ is the horizontal particle velocity at the reference water depth $z=z_\alpha$. v is a control parameter determining the nonlinearity of the equations to be used in the model, with fully nonlinear denoted by $v=1$ and weakly nonlinear denoted by $v=0$. The other quantities are defined as

$$U=u+h[b_1hu_{xx}+b_2(hu)_{xx}] \tag{11}$$

$$E=-[(h+\eta)u]_x-[a_1h^3u_{xx}+a_2h^2(hu)_{xx}]_x \tag{12}$$

$$F=-g\eta_x-uu_x \tag{13}$$

The higher order dispersive terms are defined as

$$E_2=-\left\{\left[a_1h^2\eta+\frac{1}{6}\eta(h^2-\eta^2)\right](u_{xx})\right\}_x-\left\{\left[a_2h\eta-\frac{1}{2}\eta(h+\eta)\right](hu)_{xx}\right\}_x \tag{14}$$

$$F_2 = -\left\{\frac{1}{2}(z_\alpha^2 - \eta^2)uu_{xx}\right\}_x - \left\{(z_\alpha - \eta)u(hu)_{xx} - \frac{1}{2}[(hu)_x + \eta(u_x)]^2\right\}_x \quad (15)$$

$$F^t = \left\{\frac{1}{2}\eta^2 u_{xt} + \eta(hu_t)_x\right\}_x \quad (16)$$

F_{br} denotes the wave breaking term, F_b the term due to bottom friction and F_{sp} is the sponge layer term. $f(x, t)$ is the source function term used to generate waves internally in the model, and

$$a_1 = \frac{1}{2}\beta^2 - \frac{1}{6}, \quad a_2 = \beta + \frac{1}{2},$$
$$b_1 = \frac{1}{2}\beta^2, \quad b_2 = \beta \quad (17)$$

where $\beta = z_\alpha/h = -0.531$. Even though amplitude dispersion and nonlinear effects become pronounced in the nearshore region and can only be modeled accurately by including nonlinear terms in the hydrodynamic equations, we first consider a simpler sub-set of the above equations to develop a corresponding set of linearized Boussinesq inversion equations.

2.3.1. Linearized Boussinesq equations

Nwogu's weakly nonlinear Boussinesq equations are found by setting $v = 0$ in Eqs. (9) and (10). If we disregard the wave breaking, bottom friction, sponge layer and source function terms, linearize the resulting equations, replace the time derivatives with the space derivatives as in Section 2.2, and integrate along x, we arrive at the linearized time-independent mass and momentum inversion equations

$$C\eta = hu + a_1 h^3 u_{xx} + a_2 h^2 (hu)_{xx} \quad (18)$$

$$\frac{g\eta}{C} = u + h[b_1 hu_{xx} + b_2 (hu)_{xx}] \quad (19)$$

The integration constants in the above equations have been neglected and are discussed in the next section. The only difference between the above equations and the shallow water inversion Eqs. (7) and (8), with the integration constants neglected, lie in the dispersive terms included here.

2.3.2. Fully nonlinear extended Boussinesq equations

Starting with the fully nonlinear extended equations and proceeding in a similar function, but keeping all the nonlinear terms, we get the fully nonlinear inversion equations. The mass equation is

$$\frac{C\eta}{h + \eta} = Pu + Qu_x + Ru_{xx} \quad (20)$$

where

$$P = 1 + \left(-\frac{\eta}{2} + a_2 h\right)h_{xx}$$

$$Q = 2\left(-\frac{\eta}{2} + a - 2h_x\right)$$

$$R = a_1 h^2 + \frac{\eta(h - \eta)}{6} + \left(-\frac{\eta}{2} + a_2 h\right)h$$

The momentum equation is

$$Lu + Mu_x + Nu_{xx} = S - g\eta \quad (21)$$

where

$$L = 1 + b_2 hh_{xx}$$

$$M = 2b_2 hh_x - \eta h_x$$

$$N = h^2 b_1 + b_2 h^2 - \frac{\eta^2}{2} - \eta h$$

$$S = \left[-\frac{u^2}{2} - \left\{\frac{1}{2}(z_\alpha^2 - \eta^2)uu_{xx}\right\} - \left\{(z_\alpha - \eta)[u(hu)_{xx}]\right\} - \frac{1}{2}\left\{[(hu)_x + \eta u_x]^2\right\} - g\eta\right]\frac{1}{C}$$

where all the nonlinear terms involving velocity have been collected in S. We now have the time-independent mass and momentum equations which will be used in Section 3 to formulate the depth inversion algorithm in the absence of mean flow effects.

2.4. Including mean flow effects

The inversion equations derived above cannot account for currents, since the integration constants involving the mean flow quantities were neglected. Due to this, with respect to a stationary frame of reference, the wave would appear to travel faster on a following current and slower on an opposing current. This shift in the phase speed would be inferred as a corresponding (but spurious) change in the bathymetry in the present set of depth inversion equations. To show how to correctly model mean flow effects, let us consider the nonlinear shallow water equations, which, after replacing the time derivatives with the spatial derivatives, can be integrated along x, to arrive at

$$-C\eta + [u(h+\eta)] = A_2 \tag{22}$$

$$-Cu + \frac{u^2}{2} + g\eta = B_2 \tag{23}$$

We can split the total surface elevation and orbital velocity as

$$\eta = \eta_w + \bar{\eta},\ \ u = u_w + \bar{u} \tag{24}$$

where subscript w denotes the oscillatory part and the overbar –, the mean part of a quantity. Substituting in the mass and momentum equations, we get

$$\begin{aligned} &- C(\eta_w + \bar{\eta}) + u_w(h + \eta_w + \bar{\eta}) + \bar{u}h + \overline{u\eta} \\ &\quad + \bar{u}\eta_w = A_2 \end{aligned} \tag{25}$$

$$\begin{aligned} &- C(\bar{u} + u_w) + \left(\frac{\bar{u}^2 + u_w^2}{2} + \bar{u}u_w\right) + g\bar{\eta} \\ &\quad + g\eta_w = B_2 \end{aligned} \tag{26}$$

The integration constants A_2 and B_2 can be determined by considering the case when waves are absent, in which case

$$A_2 = \bar{u}(h + \bar{\eta}) \tag{27}$$

$$B_2 = \frac{\bar{u}^2}{2} + g\bar{\eta} \tag{28}$$

Consider the case when total velocity data are available. The surface elevation and depth are unknown. The mean flow is a time averaged quantity by definition, but since time series of velocity data are not available (only spatial information at two time instances is given), we calculate the current from the total velocity by locally averaging in space over each individual wavelength. This would be exact for a strictly periodic wave in space and time. After calculating $\bar{u}$ and assuming a weak current ($\bar{\eta} \approx 0$), the wave part of the elevation and velocity is calculated by

$$u_w = u - \bar{u},\ \ \eta_w \approx \eta \tag{29}$$

Since Eqs. (22) and (23) involve both the wave and mean parts of the variables (because of which $A_2 \neq 0$ and $B_2 \neq 0$), we formulate the corresponding equations valid only for the pure wave part

$$-C_0\eta_{1_w} + u_{1_w}(h + \eta_{1_w}) = 0 \tag{30}$$

$$-C_0 u_{2_w} + \frac{u_{2_w}^2}{2} + g\eta_{2_w} = 0 \tag{31}$$

where $C = C_0 + \bar{u}$ is the Doppler shifted phase speed. It is to be noted that A_2 and B_2 have not been neglected but cancel out with the mean quantities in the mass and momentum equations. The phase speed C_0 can be estimated from the spatial maps of the pure wave part of the total velocity, or by subtracting the Doppler shift effect, which is essentially the current, from the phase speed estimated from the total velocity profiles. If on the other hand, mean flows are present and only surface elevation data are given in the form of spatially dense profiles, the determination of the pure wave quantities remains ambiguous. The mean currents cannot be determined from elevation data and neither can they be neglected in favor of the mean water level changes. The present modification for mean flow effects to the inversion method can thus only be performed with velocity data. The Boussinesq inversion equations including mean flow effects remain the same as in Sections 2.3.1 and 2.3.2, except that the pure wave quantities have to be used in the equations as shown above.

3. Inversion algorithm

We now have a set of two time-independent inversion equations, involving the surface elevation, the particle velocity, the phase speed and the water depth. One of the two particle kinematics and the phase speed is known. The water depth and the other kinematic variable are unknown. In this section, we formulate the solution algorithm for each set of equations depending on the type of surface information available as input data. The linearized algorithm, owing to its simplicity, is then discussed in detail through a simple test case.

Consider the time-independent linearized shallow water inversion equations

$$-C\eta_1 + hu_1 = 0 \tag{32}$$

$$-Cu_2 + g\eta_2 = 0 \tag{33}$$

in the absence of mean flows. 1 and 2 are the subscripts used to denote variables in the mass and momentum equation, respectively. This convention will be followed through the rest of this paper. Based on the type of data availability, we can differentiate two separate cases—CASE I, when only surface elevation data (η) are given and CASE II, when only particle velocity data (u) are given. Consider first CASE I. The ratio of velocities obtained from the mass and momentum equations is

$$\frac{u_1}{u_2} = \frac{C^2}{gh}\frac{\eta_1}{\eta_2} \tag{34}$$

Since the water depth is also unknown, a flat bottom of arbitrary depth throughout the domain is fixed as a first guess. Let this be denoted as h_0 ($h_0 = 2m$). The still water level is at $z = 0$. We then substitute the elevation data into the mass and momentum equations so that $\eta_1 = \eta_2 = \eta$. The computed phase speed is expressed in terms of the shallow water depth as $C^2 = gh_{sh}$, where the shallow water depth (h_{sh}) is the first estimate in the inversion. On substituting for C in terms of h_{sh} into Eq. (34), we get

$$\frac{u_1}{u_2} = \frac{h_{sh}}{h_0} \tag{35}$$

Fig. 1(a) shows the mismatch in the velocities calculated from the mass and momentum equations. The actual, starting, and inverted depths are shown in the bottom panel. It can be seen that wherever the

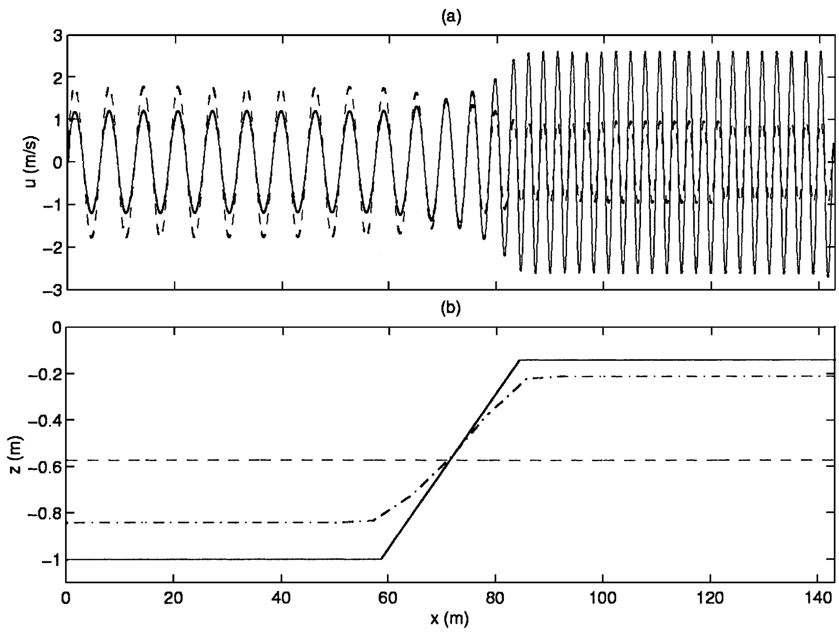

Fig. 1. (a) Velocities calculated for the first estimate of depth ($h_{new} = h_{sh}$). u_1 (- -) and u_2 (—). (b) Actual (—), starting (- -) and first inverted (-·) bottom elevations.

inverted depth is less than the actual depth, u_1 is greater than u_2 and vice versa. A new estimate of depth (h_{new}) would be given (based on this velocity mismatch) as

$$h_{\text{new}} = h_{\text{sh}}\left(\frac{u_1}{u_2}\right) \tag{36}$$

The depth is iteratively updated until the ratio of velocities calculated from the mass and momentum equations approaches unity.

Consider the alternate inversion case, when only particle velocity (u) is given over the domain (CASE II). Then, since $u_1 = u_2 = u$,

$$\frac{\eta_1}{\eta_2} = \frac{h_0}{h_{\text{sh}}} \tag{37}$$

Starting from a flat bed, a new depth estimate can thus be obtained from

$$h_{\text{new}} = h_0\left(\frac{\eta_2}{\eta_1}\right) \tag{38}$$

As before, the depth is updated till the ratio of surface elevations approaches unity.

3.1. Linearized inversion equations

The above method can similarly be applied to the Boussinesq equations to increase the range of applicability of the inversion process to include dispersive and nonlinear effects. From Section 2.3.1, the linearized inversion equations based on Nwogu's linearized extended Boussinesq equations are

$$\eta_1 = \frac{hu_1 + a_1 h^3 u_{1_{xx}} + a_2 h^2 (hu_1)_{xx}}{C} \tag{39}$$

$$\eta_2 = \frac{\{u_2 + h[b_1 h u_{2_{xx}} + b_2 (hu_2)_{xx}]\}C}{g} \tag{40}$$

Let us first consider the mathematically simpler CASE II. Central finite differences ($O(\Delta x)^2$) are used to calculate the spatial derivatives. It is to be noted that u_1 and u_2 here do not represent the data from two separate profiles. The subscripts are merely used to differentiate the variable in the mass and momentum equations. The depth is updated as

$$h_{\text{new}}(j) = h_{\text{old}}(j)\left(\frac{\displaystyle\sum_{i=j-W/2}^{i=j+W/2} |\eta_2(i)|}{\displaystyle\sum_{i=j-W/2}^{i=j+W/2} |\eta_1(i)|}\right)^{\beta} \tag{41}$$

where β is a kind of shallowness parameter, similar to the one used by Kennedy et al. (2000b) in their depth updating algorithm. $\beta = 1$ leads to the shallow water estimate of the depth. i and j denote spatial grid positions. $h_{\text{old}} = h_0$ and $h_{\text{new}} = h_{\text{sh}}$ in the first iteration of depth. W has to be approximately on the order of a wavelength to reduce numerical noise and provide enough wave information within the window. The mismatch in surface elevations calculated from the two equations is used as a convergence criterion to stop the iteration process. The total error over the entire domain is defined as

$$\epsilon = \sum_{i=1}^{i=N}\{\,|\,|\eta_1(i)| - |\eta_2(i)|\,|\,\} \tag{42}$$

where N is the total number of grid points in the domain. Theoretically, the true value of the error, when the iterated depth converges to its final value, should be $\epsilon = 0$. However, because of approximations in the solution, such as a linear interpolation over the domain and the waveform not being exactly stationary, the mass and momentum equations cannot be solved to give exact values of the elevations. The error ϵ therefore always is a finite nonzero quantity. Since a minimum error also cannot be predefined (because the true surface elevation is an unknown quantity), the iteration is terminated when the error approaches a constant value within a predefined arbitrary tolerance. Fig. 2 shows the total mismatch between the calculated surface elevations summed over the domain, plotted against the number of iterations for the linearized case. Based on previous model runs, the maximum number of iterations for this case was fixed at nine. The error

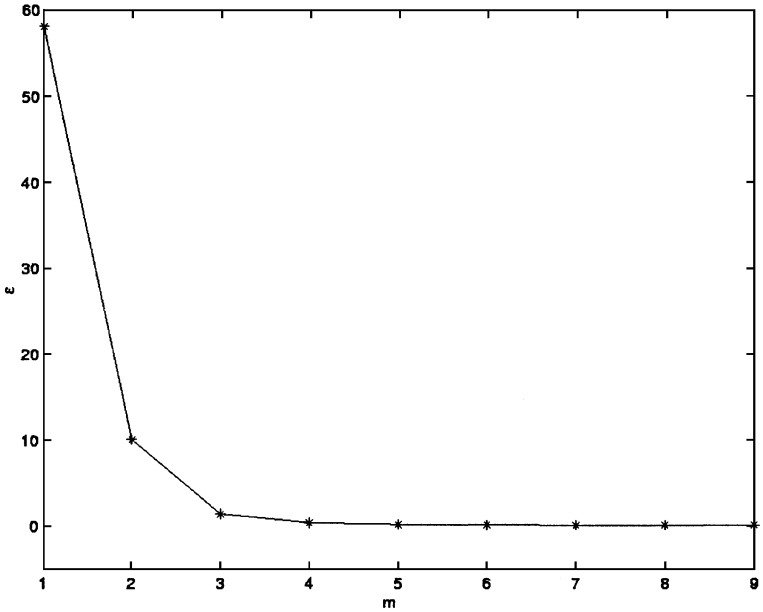

Fig. 2. The total mismatch of surface elevations (ϵ) at successive iterations (m) in the linearized inversion case.

drops to its minimum constant value after about five to six iterations. The algorithm converges to a final depth and surface elevation estimate within a few seconds of computational time.

For CASE I, the inversion problem reduces to solving the mass and momentum equations for $u(x)$ and $h(x)$. The linearized inversion equations can be recast in the following manner

$$u_1[h + a_2h^2h_{xx}] + u_{1_x}[a_2h^2 2h_x] + u_{1_{xx}}[(a_1 + a_2)h^3] = C\eta_1 \tag{43}$$

$$u_2[1 + b_2hh_{xx}] + u_{2_x}[2b_2hh_x] + u_{2_{xx}}[(b_1 + b_2)h^2] = \frac{g\eta_2}{C} \tag{44}$$

The linearized mass and momentum equations are solved using centered finite differences. Boundary values are needed for the unknown, which here are the unknown particle velocities u_1 and u_2. We arbitrarily set the values $u_1(1) = u_1(N) = 0$ and $u_2(1) = u_2(N) = 0$. This approximation has been seen to affect computations only near the boundaries and does not propagate into the domain. A new estimate of depth is obtained as

$$h_{\mathrm{new}}(j) = h_{\mathrm{old}}(j)\left(\frac{\sum_{i=j-W/2}^{i=j+W/2} |u_1(i)|}{\sum_{i=j-W/2}^{i=j+W/2} |u_2(i)|}\right)^{\beta} \tag{45}$$

The total error is defined as

$$\epsilon = \sum_{i=1}^{i=N}\{\,|\,|u_1(i)| - |u_2(i)|\,|\,\} \tag{46}$$

The iteration is similarly terminated when ϵ approaches a constant value.

3.1.1. Numerical example

To test the inversion method developed above, a synthetic data set was generated from a progressive monochromatic wave with wave height $H = 0.05$ m and wave period $T = 4.37$ s, allowed to propagate over a 1:30 plane slope. The deep water depth was $h_{\mathrm{d}} = 3.5$ m, and in the shallow region, the water depth was

$h_s = 0.5$ m. The corresponding values of the dispersion parameter were $\mu_d = 0.98$ and $\mu_s = 0.33$, such that the wave was propagating in intermediate water throughout the domain. The nondimensional period can be defined as $T' = T\sqrt{\frac{g}{h_d}} = 7.31$. ν was set equal to zero in the model to simulate waves, since the analytic phase speed in this case can be obtained from Nwogu's linear dispersion relationship

$$C^2 = gh\left[\frac{1-(\alpha+(1/3))(kh)^2}{1-\alpha(kh)^2}\right] \tag{47}$$

where $\alpha = 0.39$. The aim of this example is not an attempt at inverting depth under synthetically constructed real sea conditions, but to examine the numerics of the inversion algorithm itself. The model grid spacing was d$x = 0.25$ m and the time step was d$t = 0.02$ s. The total domain length was 500 m. Sponge layers of width 25 and 50 m were applied on the seaward and shoreward boundaries, respectively. No wave breaking was observed as the wave propagated over the topography. The elevation and velocity maps were stored at six time steps t1 = 401 s, t2 = 401.5 s, t3 = 500 s, t4 = 501 s, t5 = 600 s and t6 = 602 s. Steady state wave conditions had been reached before the data were recorded. The top panel (a) in Fig. 3 shows the two surface profiles at times t5 and t6. The dashed line is the first snapshot and the solid line is the later snapshot lagged by $\delta t = 2.0$ s, which is about half the wave period. η' is the nondimensionalized surface elevation ($\eta' = (\eta/a_0)$), where $a_0 = 0.025$ m is the incident wave amplitude. Cross-shore distance ($x' = (x/h_d)$) and bottom elevation ($z' = (z/h_d)$) have been nondimensionalized by the deep water depth h_d. In all the inversion tests, the domain has been truncated to get rid of the sponge layers and parts of the uninteresting flat regions on either side of the slope.

The linear analytic phase speed is compared with the least-square estimated phase speed in the top panel of Fig. 4. The phase speeds have been nondimensionalized ($C' = (C/C_d)$) by the analytic deep water phase speed $C_d = 5.12$ m/s calculated from Eq. (47). The window size was $W = 25$ m, which is about the same as the deep water wavelength ($L_d = 22.44$ m), and the window shift was 5 m. The nondimensional window size $W' = (W/L_d) = 1.11$. The analytic

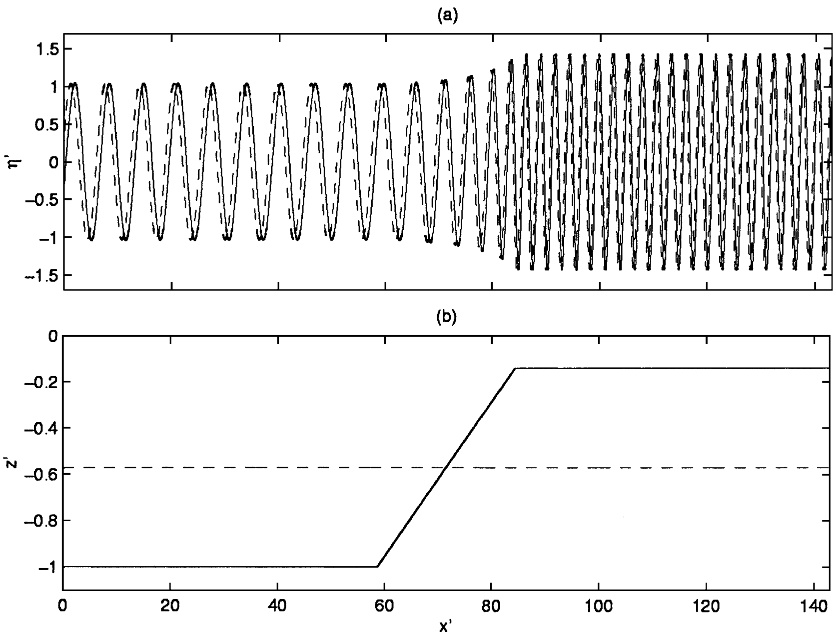

Fig. 3. (a) Wave surface profiles generated with $\nu = 0$. (b) Assumed (- -) and actual bottom elevations (—).

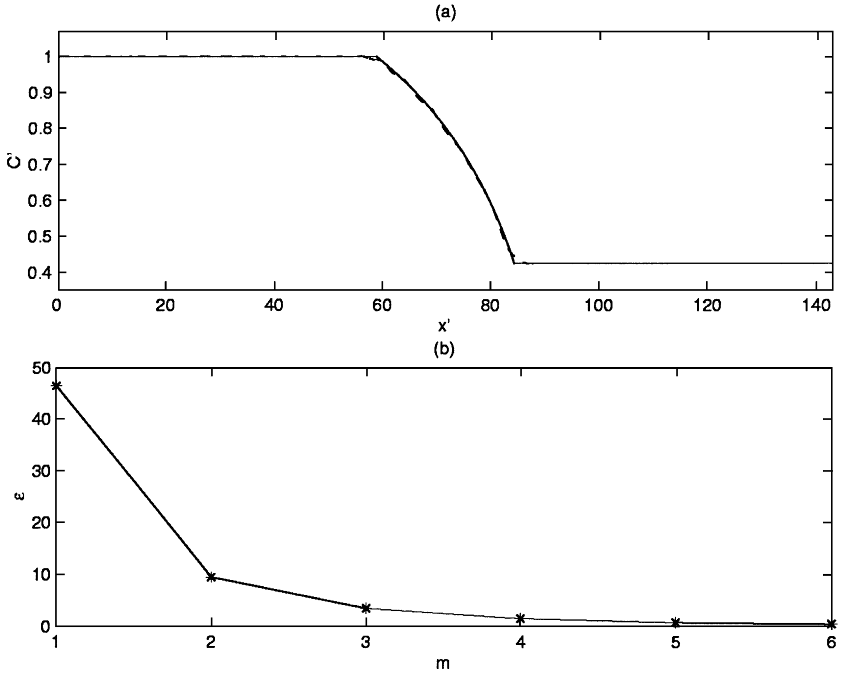

Fig. 4. (a) Analytic (—) and estimated (- -) wave phase speed. (b) Total velocity mismatch (ϵ) at successive iterations (m).

speed is estimated accurately except at the sharp corners in the bathymetry, because of the large finite window size. Convergence is fast and the error decreases monotonically to its minimum value within about five iterations. The shallowness parameter $\beta = 1.0$.

The top panel of Fig. 5 shows the final converged inverted depth compared to the actual or true depth. The depth estimate agrees well with the analytic bathymetry except at the sharp corners. The smearing in phase speed translates to a corresponding loss in resolution in the inverted depth. From Eqs. (32) and (33), for a given depth and surface elevation data, we can see that an over-prediction of phase speed leads to an over-prediction in u_1 and an under-prediction in u_2. The orbital velocities from the mass equation have been nondimensionalized as $u_1' = (u_1/(a_0 C_d = h_d))$, and similarly for u_2' and the true velocity u'. If the computed phase speed is smaller than the true phase speed, u_1 would be smaller than u, and u_2 would be greater than u. Also, from Eq. (36), it can be seen that a discrepancy in the computed velocities translates to a corresponding error in the inverted depth. For example, at the offshore toe of the slope, the phase speed is under-predicted, which leads to an under-prediction of u_1 and a corresponding under-prediction in depth.

The shallowness parameter can be increased to accelerate convergence. An increased value of β directs the depth iterates toward the true depth more quickly. However, the iteration has been observed to begin diverging at $\beta > 2.0$. For all the inversion cases, the shallowness parameter has been kept fixed at $\beta = 1.0$. To investigate the possible effect of an arbitrarily assumed starting depth on the inversion, three different initial bathymetries were considered, all of which were constant across the domain. In Fig. 6(a) are shown the three assumed depths along with the actual depth. In the bottom panel is plotted the total velocity mismatch for the different assumed starting depths. The inversion algorithm converges uniformly to the same value for all the three cases and the inverted depth and velocity estimates for inversion tests performed with the three different starting depths were the same. Any arbitrary depth can thus be used as a starting point for the inversion.

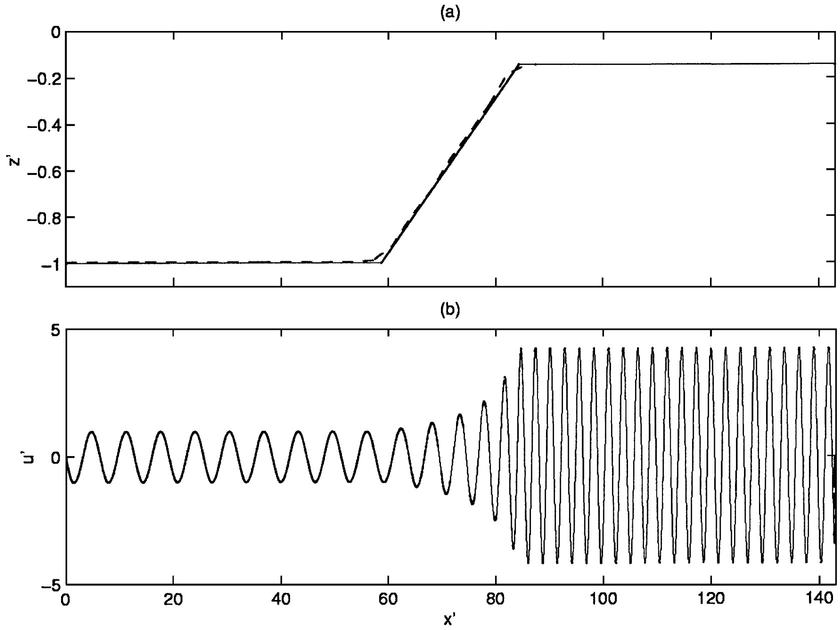

Fig. 5. (a) Actual (—) and inverted bottom elevations (- -). (b) Actual (—) and estimated velocities $\{u_1'$ (-·), u_2' (- -)$\}$.

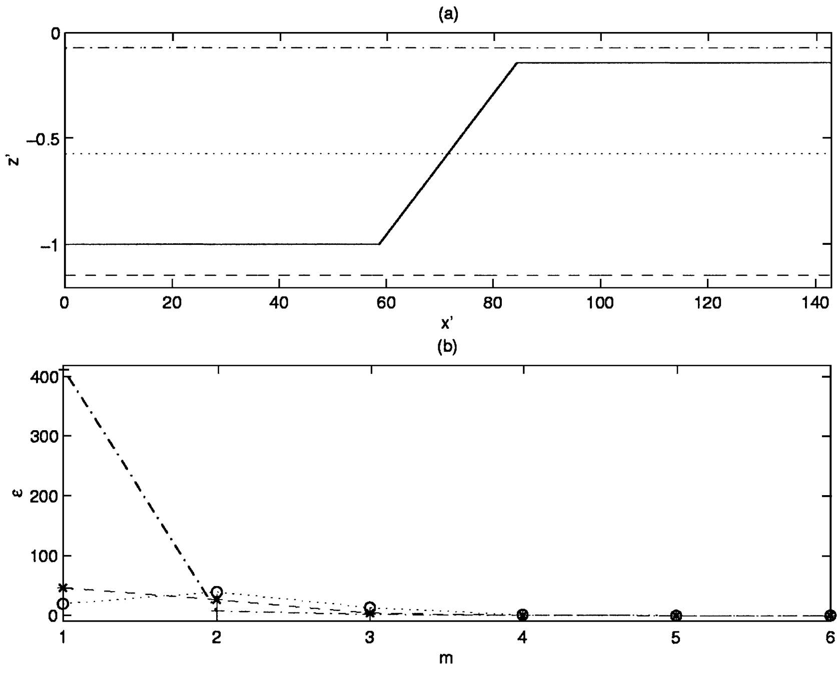

Fig. 6. (a) Actual (—) and assumed bottom elevations: z_{01}' (·), z_{02}' (-·), z_{03}' (- -). (b) Total velocity mismatch at successive iterations during inversion with the different assumed bottom elevations z_{01}' (∗), z_{02}' (+) and z_{03}' (○).

3.2. Fully nonlinear inversion equations

Let us consider CASE II first, when only velocity data are available. The mass equation can be written as

$$P_1\eta_1 + Q_1\eta_1^2 + R_1\eta_1^3 = S_1 \tag{48}$$

$$P_1 = u_1 - C + a_1h^2u_{1_{xx}} + \frac{h^2u_{1_{xx}}}{6} - \frac{h(hu_1)_{xx}}{2} + a_2h(hu_1)_{xx}$$

$$Q_1 = -\frac{(hu_1)_{xx}}{2}$$

$$R_1 = -\frac{u_{1_{xx}}}{6}$$

$$S_1 = -a_1h^3u_{1_{xx}} - hu_1 - a_2h^2(hu_1)_{xx}$$

The momentum equation can be written as

$$P_3\eta_2 + Q_3\eta_2^2 = S_3 \tag{49}$$

$$P_3 = g - u_2(hu_2)_{xx} + (hu_2)_xu_{2_x} + Ch_xu_{2_x} + Chu_{2_{xx}}$$

$$Q_3 = -\frac{u_2u_{2_{xx}} + u_{2_x}^2 + u_{2_{xx}}C}{2}$$

$$S_3 = C[u_2 + h^2u_{2_{xx}}(b_1 + b_2) + b_2hh_{xx}u_2 + 2b_2hh_xu_{2_x}] - \frac{u_2^2}{2} - \frac{z_\alpha^2u_2u_{2_{xx}}}{2} - z_\alpha u_2(hu_2)_{xx} - \frac{(hu_2)_x^2}{2}$$

The momentum equation is quadratic in the unknown η_2 and has standard analytic solutions. Since there exists more than one solution for both the mass and momentum equations (the equations being cubic and quadratic), of which only one is the correct value, and since solving the mass equation using standard analytical solutions involves evaluating complex quantities, a simpler solution procedure using Newton Raphson method was used. The Newton Raphson method requires an initial guess or a seed value, which in this case was provided by first solving the linearized mass and momentum (Eqs. (39) and (40)), and then substituting the solution as an initial guess to solve Eqs. (48) and (49). The iteration of depth remained the same, based on the mismatch between the calculated values of η_1 and η_2.

The inversion procedure for CASE I can be formulated by rewriting the fully nonlinear inversion equations in terms of the unknown velocities u_1 and u_2. The mass equation is

$$L_1u_1 + M_1u_{1_x} + N_1u_{1_{xx}} = \frac{C\eta_1}{h+\eta_1} \tag{50}$$

$$L_1 = 1 + \left(-\frac{\eta_1}{2} + a_2h\right)h_{xx}$$

$$M_1 = 2\left(-\frac{\eta_1}{2} + a_2h\right)h_x$$

$$N_1 = a_1h^2 + \frac{\eta_1(h-\eta_1)}{6} + \left(-\frac{\eta_1}{2} + a_2h\right)h$$

The momentum equation is given by

$$L_2u_2 + M_2u_{2_x} + N_2u_{2_{xx}} = \frac{K_2 - g\eta_2}{C} \tag{51}$$

$$L_2 = 1 + b_2h^2h_{xx}$$

$$M_2 = 2b_2hh_x - \eta_2h_x$$

$$N_2 = h^2(b_1 + b_2) - \frac{\eta_2^2}{2} - \eta_2h$$

$$K_2 = \left[-\frac{u_2^2}{2} - \left\{\frac{1}{2}(z_\alpha^2 - \eta_2^2)u_2u_{2_{xx}}\right\} - \left\{(z_\alpha - \eta_2)[u_2(hu_2)_{xx}]\right\} - \frac{1}{2}\left\{[(hu_2)_x + \eta_2u_{2_x}]^2\right\}\right]$$

The mass equation is solved with boundary values for u_1 and u_2 set to zero. The left hand side of the momentum equation is also tridiagonal in u_2, but the term K_2 contains nonlinear convective terms involving the unknown u_2 itself. The momentum equation is thus solved iteratively. At the first iteration, all the nonlinear terms in u_2 are neglected ($K_2=0$) and the following linear equation is solved for u_2

$$L_2u_2 + M_2u_{2_x} + N_2u_{2_{xx}} = -\frac{g\eta_2}{C} \tag{52}$$

The solution to Eq. (52) is used to calculate K_2. K_2 is then substituted into Eq. (51) to calculate the solution to the fully nonlinear equation. Based on the mismatch between u_1 and u_2, the depth is updated as before.

4. Results

4.1. Inversion with surface elevation data (CASE I)

Two different types of surface elevation data from the fully nonlinear time-dependent Boussinesq model have been considered, one in which there were no prescribed mean flows (CASE IA), and the second in which an initial mean current was prescribed (CASE IB) in the model.

4.1.1. No prescribed mean flows in surface elevation data (CASE IA)

There were no prescribed mean flows in CASE IA, i.e. $\bar{\eta}=0$ and $U=0$. The deep water wave height was $H=0.12$ m and the fully nonlinear model was run to simulate the waves. The bathymetry and other model parameters remained the same as in Section 3.1.1. Since the wave evolves in time because of nonlinear effects, the estimates of phase speed vary depending on the time instants at which the waveforms are recorded. Therefore, the assumption in the inversion methodology, that the first profile can be translated to the second by the spatially varying but temporally constant phase speed $((\partial/\partial t)\rightarrow C(\partial/\partial x)$, $(\partial^2/\partial t^2)\rightarrow C^2(\partial^2/\partial x^2))$ is no longer valid. Profiles were recorded at 50 random time instances spanning about 18 wave periods. A second set of 50 profiles was recorded 0.5 s after the first set. A pair of snapshots is shown in Fig. 7(a). Phase speeds were estimated for each pair of profiles, with the window size and the window shift being 15 m. The error bar plot in Fig. 8 shows the

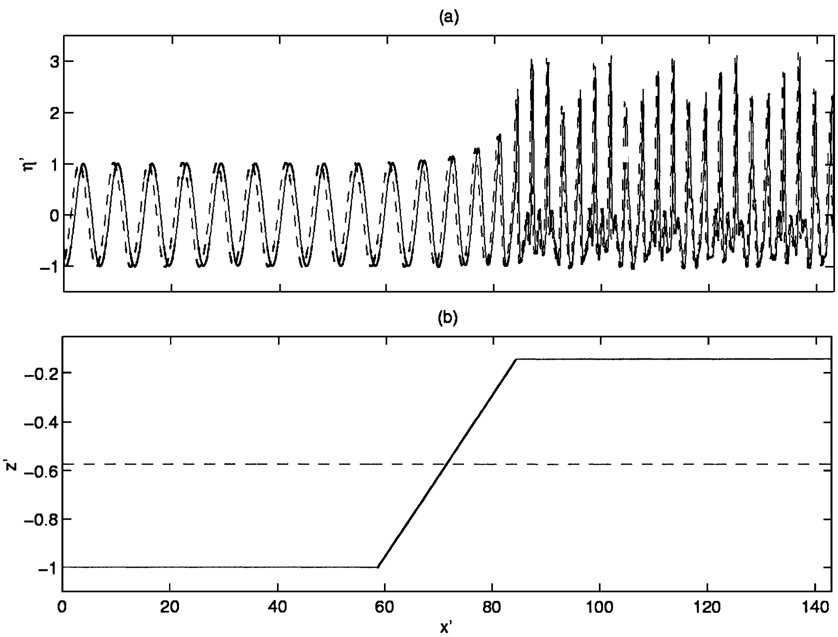

Fig. 7. (a) Surface elevation profiles for CASE IA ($\nu=1$). (b) Actual (—) and assumed bottom elevation (- -).

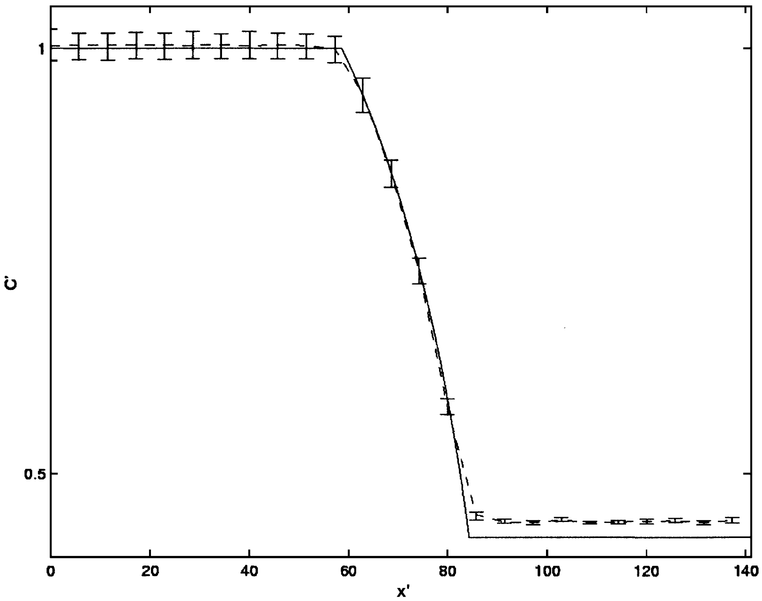

Fig. 8. Error bar plot of estimated (- -) and analytic (—) phase speeds.

maximum variation of the phase speed estimates, which are randomly distributed about the analytic value in the deeper part of the slope, while in the shallower region, they are consistently larger. The average phase speed is shown as the dashed line. Inversion was done with both the linearized and fully nonlinear inversion equations and the depth and particle velocity estimates were averaged. The inverted depths are shown in Fig. 9(a). The percentage error E_h for the estimated depth can be defined as

$$E_h(x) = \left[\frac{h_{\mathrm{est}}(x) - h(x)}{h(x)}\right] \times 100 \qquad (53)$$

and is shown in Fig. 9(b). In Eq. (53), $h_{\mathrm{est}}(x)$ and $h(x)$ are the estimated and actual depths, respectively. In the deeper part of the slope, the inverted depths are indistinguishable from the actual depth. As the wave shoals up the slope, the nonlinearity increases, and in the shallowest region, the error in the linearized inverted depth is larger than the fully nonlinear estimate by about 10%. The estimated velocities from the fully nonlinear mass and momentum inversion equations agree well with the actual value and are shown in Fig. 10. The over-prediction of the phase speed causes the over-prediction in the mass velocity and correspondingly, an over-prediction of depth.

To further test the limitation imposed by our assumptions, we simulate the experiments performed by Beji and Battjes (1993) in the fully nonlinear Boussinesq model. The bar is shown in Fig. 11(a), with the dashed line denoting the assumed depth for the fully nonlinear inversion computations. The incident wave characteristics for the test case considered here were $T = 2.02$ s and $H = 0.02$ m, $\mu = k_0 h_0 = 0.67$ and $\delta = (H/2h_0) = 0.025$. The waves remained unbroken throughout the simulation. Previous computations and comparisons with experimental data (Gobbi and Kirby, 1999) have shown that the fully nonlinear extended Boussinesq equations can predict the wave evolution for this case with reasonable accuracy. Fifty profiles were recorded at random time instances spanning about nine wave periods. Each of the second set of 50 profiles were collected 0.1 s after the first snapshot, $\delta t = 0.1$ s. The time-lag ($\delta t \approx (T/20)$) was kept small since the wave evolves very quickly in time. The first pair of waveforms are shown in Fig. 11(b), with the dashed line being the first profile in time. Fig. 12(a) shows the linear analytic and estimated phase speeds. A window with $W' = 0.53$ was used to calculate local estimates of the phase speed. As the wave propagates over the bar, almost all the energy associated with the primary

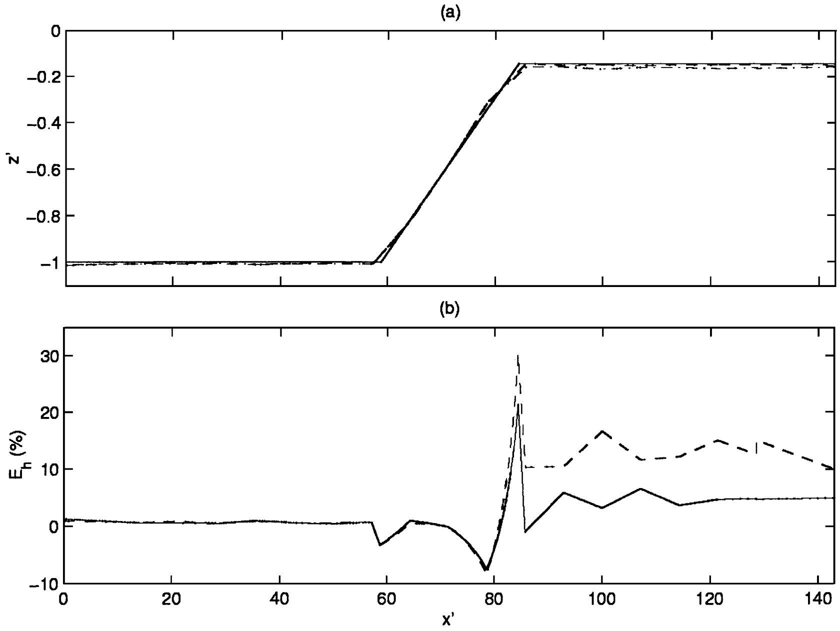

Fig. 9. (a) Actual (—) and estimated depths. Linearized inversion (-·), fully nonlinear inversion (- -). (b) Percentage error of estimated depths. Linearized inversion (- -), fully nonlinear inversion (—).

wave is transferred to the second and third harmonics. The primary wave and the harmonics travel at different speeds in this region and the resulting wave signature is fairly complicated. Before the bar, since nonlinearity is not so pronounced, it is the fundamental wave which has all the energy and represents

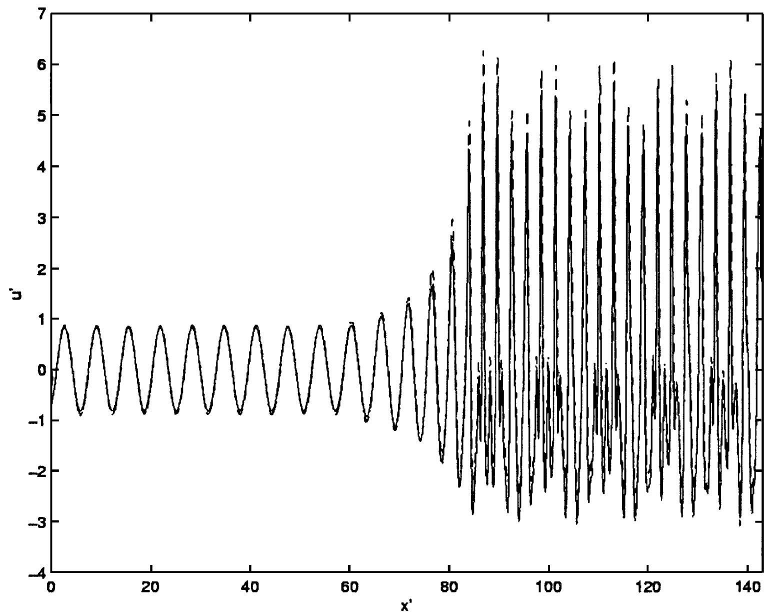

Fig. 10. Actual (—) and estimated velocities u_1' (-·), u_2' (- -) with fully nonlinear inversion.

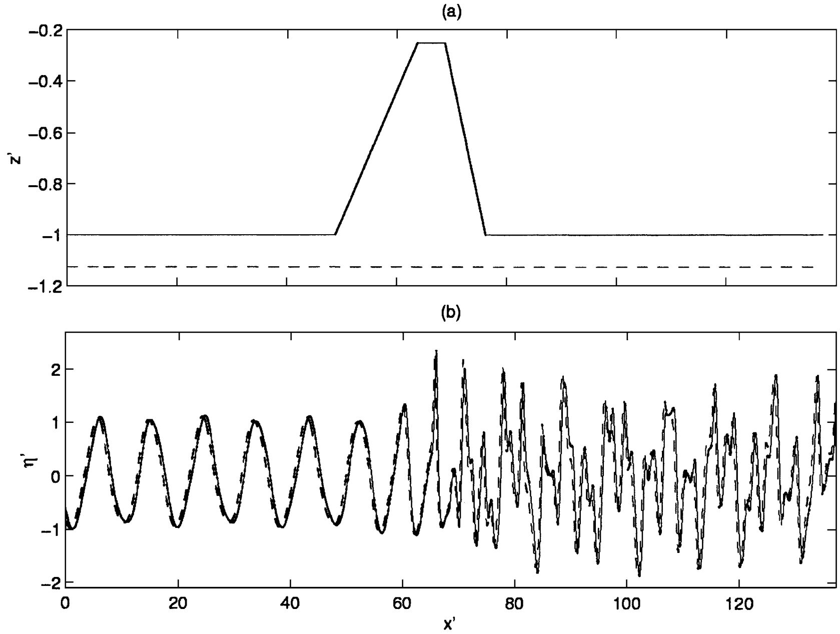

Fig. 11. (a) Actual (—) and assumed bottom elevation (- -). (b) Wave surface elevation profiles ($\nu = 1.0$).

by itself the wave train. The estimated phase speeds are distributed evenly about the analytic linear phase speed for the primary wave in this region. After the bar, the estimated values lie between the individual phase speeds of the second and the third harmonics. This is expected since these harmonics are the dominant wave components in this region. The fully nonlinear inverted depths for the first set of profiles are plotted along with the actual depth in Fig. 12(b). The actual depth is predicted well (after averaging the inverted estimates) till the top of the bar. After the bar, since the estimated phase speeds are smaller than that of the primary wave component, the predicted depth is also shallower. The reason for this discrepancy is because of the inherent lack of time domain information in the least squares as well as the depth inversion algorithms. The estimates of local phase speeds from a given pair of profiles assumes that the waveform remains unchanged during that time interval. The broad-banded wave train in this particular case, which evolves very fast with time, violates that assumption. The local phase speed within a given window is calculated by identifying the spatial lag at which the least-squares error for the two profiles is a minimum. The magnitude of this error should theoretically be zero for a permanent form wave (see Appendix A.2). It can be seen in Fig. 13 that the error becomes very large after the top of the submerged bar when the wave becomes unsteady. The least-squares error has been nondimensionalized by the square of the incident wave amplitude ($\epsilon' = (\epsilon/a_0^2)$). The error decreases with window size, but the phase speed estimates become noisy and unreliable since wave information within the window also decreases. As expected, the error increases with the time-lag because of the evolving waveform. The time-lag was chosen as 0.1 s since, for $\delta t < 0.1$ s, the translational displacements within such a short time interval are very small and the phase speed could not be accurately estimated.

In reality, the nearshore wave field is rarely monochromatic. To simulate irregular wave conditions, several input time series were generated from a TMA spectrum program. The peak frequency ($f_p = (1/T_p)$) was 0.229 s^{-1}, nondimensionalized as $f_p' = f_p\sqrt{\frac{h_d}{g}} = 0.134$. The maximum frequency ($f'_{max} = 0.3$). The significant wave height (H_s) was 0.04 m. The actual bathymetry is the same as before and fully nonlinear

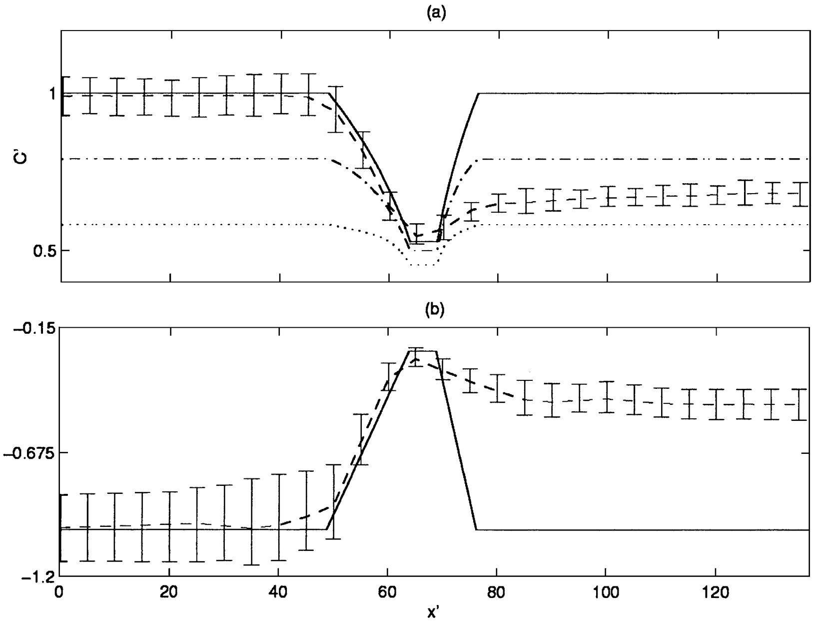

Fig. 12. (a) Linear phase speeds for fundamental wave (—), second harmonic (-·), third harmonic (·), error bar plot for estimated phase speeds and the averaged value (- -). (b) Actual (—) and error bars for estimated bottom elevations for the first set of profiles, Averaged estimated depth (- -).

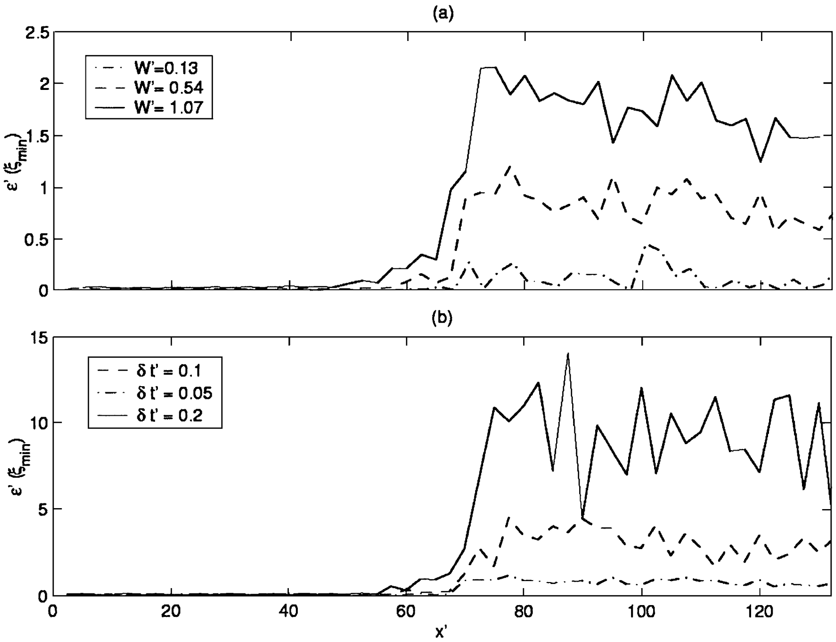

Fig. 13. (a) The nondimensionalized minimum least squares phase speed error (ϵ' ($\xi_{\min}$)) for a time lag of $\delta t' = 0.05$ and for different window sizes. (b) $\epsilon'(\xi_{\min})$ for $W' = 0.54$ and for different time lags.

Table 1
Nondimensionalized root mean square errors for estimated depths (ϵ_h) for different values of the peak enhancement factor (γ)

γ	0.5	1.0	2.0	3.0	6.0	10.0	20.0	50.0	100.0	1000.0
ϵ_h	13.62	13.62	13.29	12.99	11.98	11.99	8.62	5.72	4.30	1.30

equations were used to simulate waves. Ten tests were conducted by varying the value of the peak enhancement factor γ in the input TMA spectrum. As γ increases, the wave train becomes more broad-banded and irregular. The values of chosen are shown in Table 1. Two sets of 50 profiles, each spanning about 43 peak periods, were recorded at 50 random time instances. Each profile in the second set was lagged from the first by $\delta t' = 0.114$. The first pair of profiles for $\gamma = 0.5$ and $\gamma = 200.0$ are shown in Fig. 14. Fig. 15(a) shows the average estimated phase speed for three different values of γ. The percentage error in the average (over the first set) inverted depths is shown in the bottom panel.

The inverted depths converge to the true depth in the shallower part, but are biased toward smaller values in the deeper part ($E_h < 0$). The large errors near $x' = 60$ and $x' = 80$ are because of the sharp corners in the actual bathymetry, where the phase speed estimates are smeared by the finite sized windows. The nondimensional RMS error in the depth over the entire domain can be defined as

$$\epsilon_h = \left[\sqrt{\frac{\sum_{i=1}^{N} (h_{\mathrm{est}}(i) - h(i))^2}{N}} \right] \times \frac{100}{h_{\mathrm{d}}} \tag{54}$$

where i is the spatial index and N is the total number of points in the domain. The variation of ϵ_h with γ is shown in Table 1 and Fig. 16. The RMS error increases as the wave train becomes more broad-banded, with the largest total error being 13.6% for the smallest value of $\gamma = 0.5$.

It can be shown numerically, by considering a simple wave group consisting of two sinusoidal waves, that the modulation of the waveform causes a slope in the wave envelope which increases toward the node of the wave group envelope and that the error

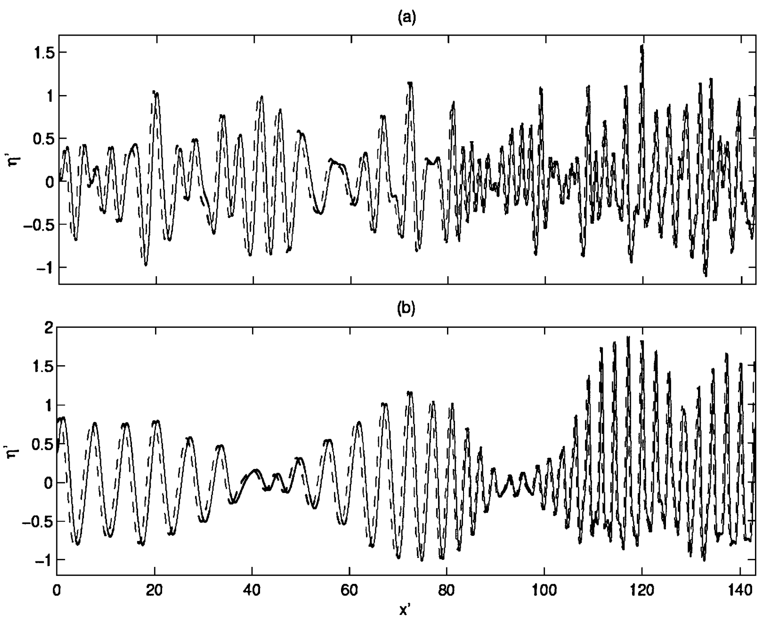

Fig. 14. (a) First profile pair $\gamma = 0.5$. (b). First profile pair for $\gamma = 1000.0$. First profile (- -), second profile (—).

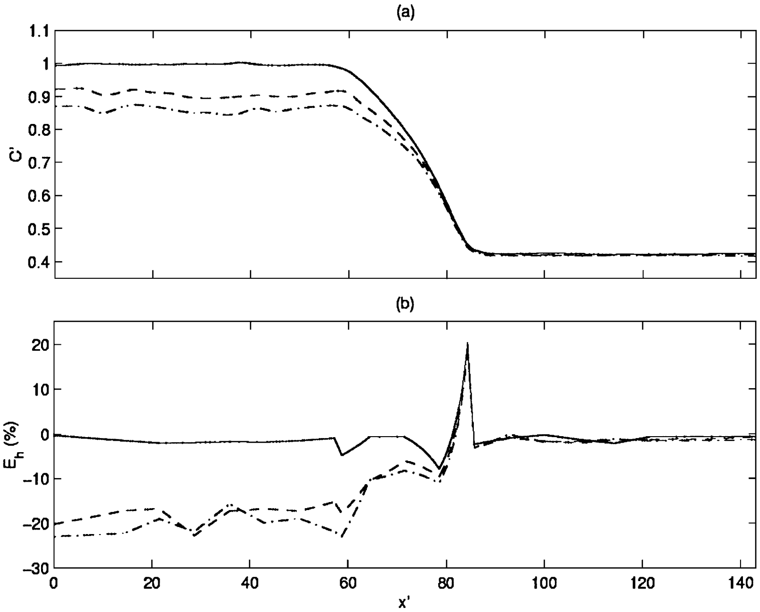

Fig. 15. (a) Averaged phase speed estimates for $\gamma = 1000$ (—), 10 (- -) and 0.5 (-·). (b) Percentage error in estimated depth for $\gamma = 1000$ (—), 10 (- -) and 0.5 (-·).

between the carrier phase speed and the computed value increases as we go from shallow to deeper water. Each time we evaluate the phase speed close to a node of the wave envelope, the estimate is in error. In the shallower part of the depth, the waves in the group are propagating at speeds independent of

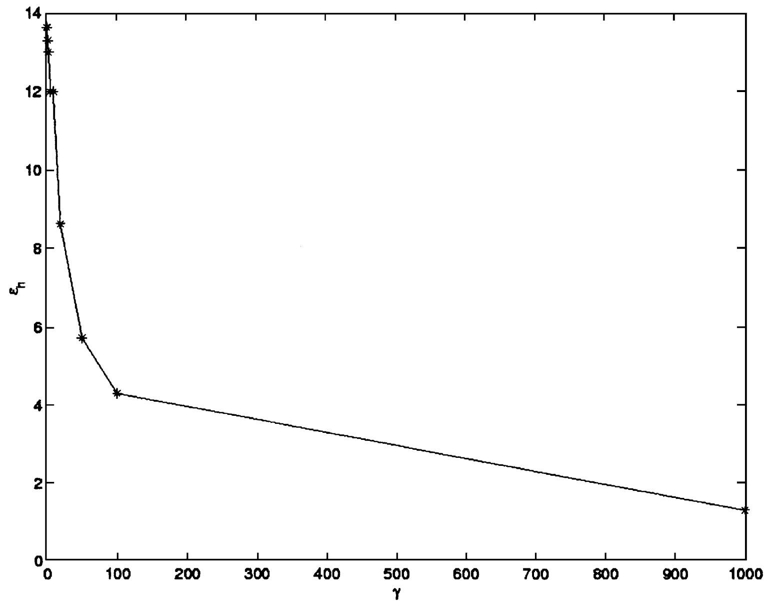

Fig. 16. Variation of nondimensionalized RMS error in inverted depth with the peak enhancement factor γ.

individual frequencies and are dependent only on the local water depth. The errors in the estimated phase speed are thus small.

4.1.2. With mean flows present in surface elevation data (Case IB)

We now consider CASE IB, where mean flows were present in the input data (spatial maps of surface elevation) and where the integration constants were neglected in the inversion equations. This test case demonstrates the errors in the estimated phase speed and inverted depth by not accounting for mean flow effects during inversion. A constant volume flux ($q_w = 0.2$ m^2/s) was specified throughout the spatial domain in the model. The resulting current is given by

$$U(x) = \frac{q_\mathrm{w}}{h(x)} \tag{55}$$

The Froude number for the mean flow ($Fr = U/\sqrt{gh}$) in the deeper part was $Fr = 0.0097$ and in the shallower shelf part $Fr = 0.1806$. The mean water level variation is small due to the weak current. Fully nonlinear extended equations were used to compute the surface maps, with the wave height $H = 0.08$ m, all other model and depth parameters remaining the same as for CASE IA. Because of the following current, the phase speed is Doppler shifted and is larger than the true phase speed. The velocity estimates are also in error. This error translates to the inverted depth and is larger in the shallower part because the current effect (magnitude) is also larger in that region of the depth. This error would increase for stronger currents. As discussed in Section 2.4, the present inversion method cannot account for mean flows with only surface elevation data, and at present, no unambiguous modifications can be suggested for CASE IB to improve depth and particle velocity predictions.

4.2. Inversion with velocity data (CASE II)

Time-lagged snapshots of particle velocity can also be used as data to estimate the depth and surface elevations. We distinguish two cases—CASE IIA, when there were no mean flows present in the data,

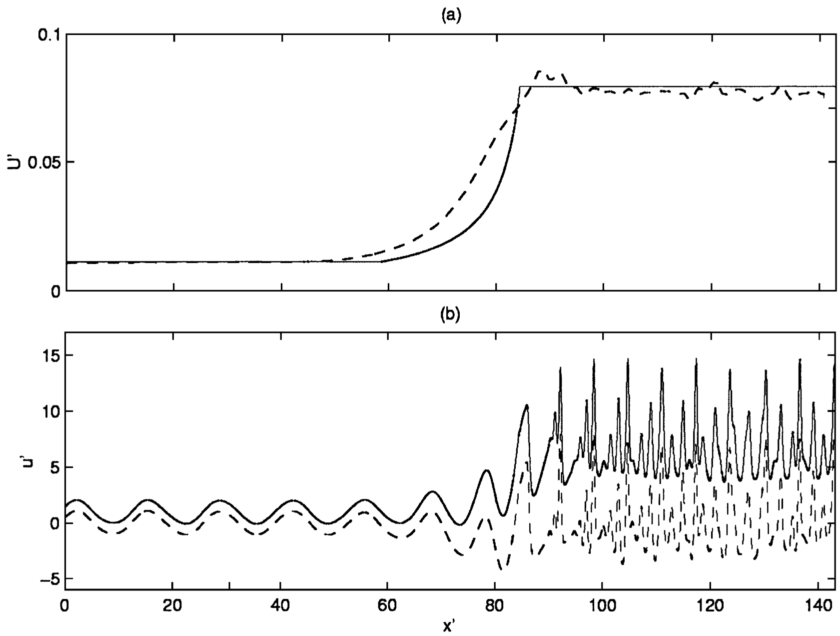

Fig. 17. (a) Prescribed (—) and estimated (- -) current profiles. (b) Biased (—) and corrected (- -) velocity input data.

and CASE IIB, when the velocity maps had prescribed mean flows in them. The inversion results for CASE IIA, as expected, are similar to those obtained from CASE IA and are not shown here.

4.2.1. With mean flows present (CASE IIB)

As before in CASE IIA, mean flows were prescribed by specifying a positive constant volume flux ($q_w = 0.2$ m^2/s) across the domain. The current is weak enough to neglect the mean water level variations ($\bar{\eta}(x)$)in the fully nonlinear inversion equations. The phase speed estimate is Doppler shifted by the current and leads to an increase due to the following current. The calculated current profile is compared to the prescribed current in Fig. 17(a). The current has been nondimensionalized by the deep water value of the linear analytic phase speed C_d. On subtracting this current from the total velocity, we get the pure wave part of the velocity, shown as the dashed line in Fig. 17(b). The Doppler shift in the phase speed is also corrected for by subtracting this current from the computed phase speed. Using the corrected phase speed and pure wave part of the velocity data, the inverted depth is calculated. The corrected estimate shows an improvement of 10% over parts of the domain as seen in Fig. 18(a). The surface elevation estimate shown as the dashed line in Fig. 18(b) is also better predicted. The errors over the slope are due to the incorrect estimate of the current profile in this region.

5. Conclusions

A depth inversion algorithm has been developed for one horizontal dimension and nonbreaking waves. The inversion input data are assumed to be in the form of time-lagged spatial profiles of either surface elevation or particle velocity. A least-squares method has been developed to compute local phase speeds from time-lagged spatial variations of either surface elevation or particle velocity. In addition to estimating the bathymetry, the inversion algorithm also computes particle kinematics, i.e. given surface elevation data, particle velocities can be calculated, and vice versa. Linearized as well as fully nonlinear

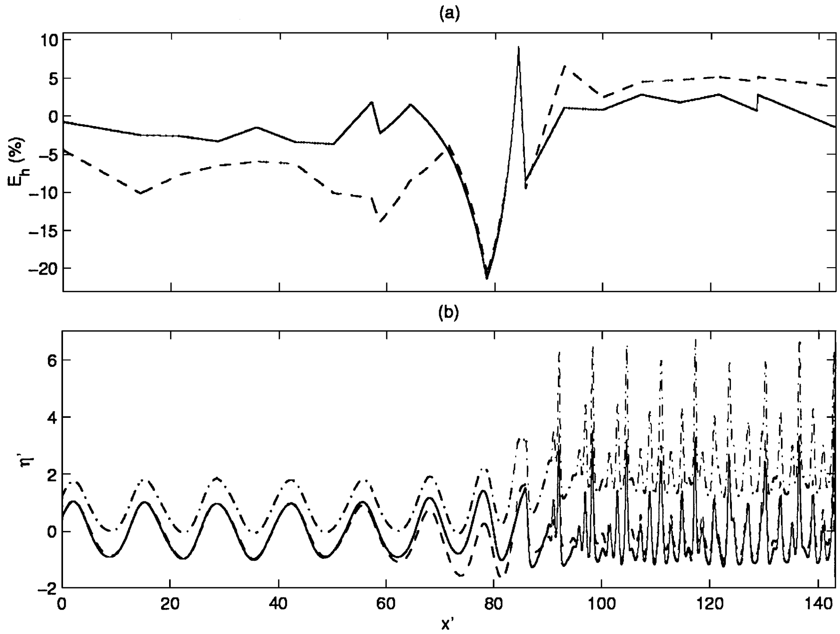

Fig. 18. (a) Percentage error in estimated depth with biased data (- -) and corrected data (—). (b) Actual (—) and estimated (biased (-·) and corrected (- -) surface elevation profiles from mass equation.

inversion equations were developed depending on the type of input data. For monochromatic wave conditions in the absence of currents, the predicted depths and particle kinematics show good agreement with actual values. For wave propagation over a (1/100) plane slope, the fully nonlinear inversion improves the depth estimates by 10% compared to the linearized inversion. In strongly nonlinear, unsteady wave conditions, such as wave propagation over a steep submerged bar, when the waveform changes in the time-lag between the two profiles, the least-squares method fails to predict the local phase speeds and leads to erroneous depth estimates. Mean flow effects due to weak currents have been included by modifying the inversion equations and for the test case considered, and improvements of 10% were found in the inverted depths. The inversion for this case can only be done with velocity data. Inversion was also done under various irregular wave conditions by varying the input TMA spectrum. The accuracy of the inverted depth deteriorated as the wave train became more broad-banded, with increased errors in the deeper part of the bathymetry. The 1-D algorithm developed here is computationally efficient, and converges for all the cases considered within a few seconds.

Acknowledgements

This work was supported by the Office of Naval Research, Base Enhancement program (Award N00014-97-1-0283).

Appendix A. Estimates of displacement

A widely used and effective method to obtain a map of the two-dimensional velocity field is Particle Image Velocimetry, where the correlation of two image patterns having a short time interval between them is used to estimate a velocity vector based on local average displacement in subregions of the overall image (Kinoshita, 1967; Keane and Adrian, 1992). By focusing over a small area in the profiles, the spatial separation giving the maximum correlation yields the local convection velocity of the particles (Utami et al., 1991). In this section, we consider a typical cross-correlation method to estimate local phase speeds from a time-lagged pair of spatial profiles of surface elevation or surface velocity. We show that the accuracy of the resulting velocity estimate is limited in cases where the spatial scale of the pattern is comparable to the analyzed snapshot dimension. We then suggest an alternate procedure based on a least-squares technique.

A.1. Conventional cross-correlation analysis

The true cross-correlation function between two stationary random processes $f(x)$ and $g(x)$ (x here denotes the horizontal spatial coordinate, $-\infty < x < \infty$) is defined as

$$\hat{R}_{fg}(\xi) = E[f(x)g(x+\xi)] \tag{56}$$

where ξ is the spatial lag between the two processes, and E stands for "the statistical expectation of". In practice, the correlation function must be estimated, since the record lengths are discrete and finite. The deterministic cross-correlation sequence based on N samples of $f(x)$ and $g(x)$ is given by

$$R_{fg}(l) = \sum_{i=0}^{N-|l|-1} f(i)g(i+l) \tag{57}$$

where we assume here that $f(i)$ and $g(i)$ are indexed from 0 to $N-1$, and $R_{fg}(l)$ from $-(N-1)$ to $(N-1)$. The wave phase speed C is calculated by first identifying the lag at which the maximum or peak value occurs in the correlation function. The peak cross-correlation value can be thought of as the maximum overlap between the two records when they are slid over each other. For a moving waveform, the lag where the peak occurs (ξ_{max}) simply means the displacement of the wave during the time interval separating the two snapshots (δt). The phase speed is then given by

$$C = \frac{\xi_{max}}{\delta t} \tag{58}$$

The phase speed estimated above is the translational velocity of the whole record, which is assumed to remain unchanged in the time interval. Willert and Gharib (1991) have noted that the average displacement vector is unbiased only if there is no velocity gradient present, that is, all particles move with the same velocity. Ocean waves on the other hand undergo spatial transformations as they propagate toward shore, and are hardly ever of a permanent form to afford such a simple analysis. There are two conflicting requirements one faces while evaluating the phase speeds at discretized positions in the spatial domain using correlation functions. Ideally, one would like to get speed estimates at every point in the domain where surface data are available. This would provide the best spatial resolution and indication of changes in celerity over space. Cross-correlation calculations (because of the need for computational efficiency) inherently require the use of fast Fourier transforms (FFTs). A periodic data set or an infinitely long (which can be assumed to have an infinite period) record would recover the analytic result because of the harmonic nature of the Fourier expansion. The finite length of the record is a drawback encountered frequently in cross-correlation techniques because there is always the risk of introducing artifacts by the implicit periodic continuation of the signal. Given two finite surface signal, however, the aim is thus to determine the phase speed at closely spaced intervals in space. The entire data are windowed by subdividing the entire domain using finite windows of length W. The window is shifted over the domain in small spatial shifts to get local estimates of the phase speed. The use of "sliding windows" has also been suggested by Roesgen and Totaro (1995) in applications where the flow field is changing slowly. The cross-correlation function for a given window is then given by

$$R_{fg}(\xi) = \frac{1}{(W-\xi)} \int_0^{W-\xi} f(x)g(x+\xi)\mathrm{d}x \tag{59}$$

Notice that the above expression yields an unbiased estimate for the cross-correlation function. In typical particle velocimetry applications, the size of the interrogation window has no direct influence on the spatial resolution since the displacement estimate reflects an average displacement of all the particle images (see Willert and Gharib, 1991). The wavelengths associated with such flow visualization applications are much smaller than the window size. In the present case, however, the window size is on the order of the wavelength. W has to be small enough to avoid smearing the local phase speed estimate within the window, and large enough to get reasonable estimates of the cross-correlation matrix.

Fig. 19(a) shows a one-dimensional (x) example calculation of phase speed from two given spatial profiles using spatial cross-correlations. The dashed and solid lines in the top panel are the surface elevation snapshots (the dashed line being the first record) of a propagating sinusoidal wave (wave period $T=8.0$ s and wavelength $L=40$ m) with a phase speed $C_{\mathrm{exact}}=5.0$ m/s, separated by a time interval $\delta t=(T/8)=1.0$ s. The two profiles are $f(x)=\cos(kx)$ and $g(x)=\cos(kx-\omega\delta t)$. k is the wave number ($k=2\pi/L$) and ω the frequency ($\omega=2\pi/T$) of the wave. The window size here is $W=100$ m. In the bottom panel is plotted the cross-correlation function R_{fg} (ξ) for the positive and negative spatial lag ξ. The cross-correlation vector has been normalized, so that the cross-correlation at zero lag is 1.0. Since it is known that the wave is propagating in the positive x direction, the positive lag at the first cross-correlation peak (ξ_{max}), is found to be $\xi_{\mathrm{max}}=4.3115$ m. ξ_{max} has been determined from the correlation vector to sub-grid accuracy by a three-point parabolic interpolation around the peak (Willert and Gharib, 1991). The phase speed as calculated from Eq. (58) is $C_{\mathrm{est}}=4.3115$ m/s. The error in the estimated phase speed is thus about 14%. The effect of a finite window size on the phase speed estimate can be seen analytically by constructing the cross-correlation for the two signals. From Eq. (59), we get

$$\begin{aligned} R_{fg}(\xi) &= \frac{1}{W-\xi}\int_0^{W-\xi} \cos(kx)\cos[k(x+\xi)-\omega\delta t] \\ &= \frac{1}{2(W-\xi)} \\ &\quad \times \left[\frac{\sin(2kW-\omega\delta t-k\xi)+\sin(\omega\delta t-k\xi)}{2k}\right. \\ &\quad \left. +(W-\xi)\cos(\omega\delta t-k\xi)\right] \end{aligned} \tag{60}$$

To identify the lag at the cross-correlation peak (the maximum value of the cross-correlation vector), we

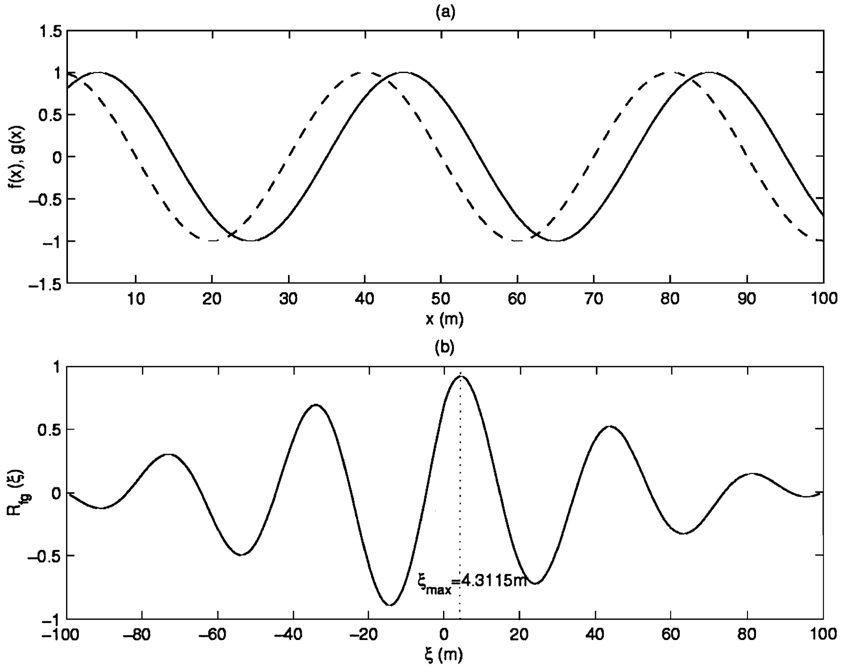

Fig. 19. (a) Wave surface snapshots lagged in time. (b) Cross-correlation vector $R_{fg}(\xi)$ calculated at varying spatial lags (ξ).

differentiate R_{fg} (ξ) with respect to the spatial lag ξ and equate it to zero.

This gives

$$\frac{\mathrm{d}R_{fg}(\xi)}{\mathrm{d}\xi} = 0 = \frac{-k(W-\xi)\cos(2kW-\omega\delta t-k\xi)+\sin(2kW-\omega\delta t-k\xi)}{2k(W-\xi)^2} - \frac{k(W-\xi)\cos(\omega\delta t-k\xi)+\sin(\omega\delta t-k\xi)}{2k(W-\xi)^2} + k\sin(\omega\delta t-k\xi) \tag{61}$$

Let the lag at the peak be $\xi=\xi_{\max}$, which can be obtained from the definition of the maximum spatial lag

$$\xi_{\max} = C\delta t = \frac{\omega}{k}\delta t \tag{62}$$

If we now substitute for $\xi=\xi_{\max}$ from Eqs. (62) into (61), we get

$$W = L\left[\frac{\delta t}{T} + \frac{(2n+1)}{4}\right] \tag{63}$$

where n is any integer. Choosing a window size and the other parameters given by Eq. (63), we would recover the exact analytic phase speed of the waveform. The expression (63) shows that, even for two perfectly sinusoidal signals, the window size is dependent upon the wavelength, the time-lag between the two signals, the time period of the wave and an integer n. This is an unfortunate result when applied to phase speed determination from two surface profiles for a number of reasons. The wavelength and the wave period are not known a priori. Real surface data also will never contain purely monochromatic waves, and thus, no unique period or length of the wave train can be determined, even if methods be available to estimate the two.

For the cosine waveform considered above, the analytic phase speed C_{ana} can be obtained by solving Eq. (61) for $\xi_{\max}$ and then dividing it by the time-lag δt. C_{ana} (nondimensionalized by the exact value), for various window sizes W (nondimensionalized by the wavelength) is shown in Fig. 20, as the dash–dot line. The dashed line is the nondimensionalized analytic phase speed obtained from two snapshots of a sine wave signal with the same wave period and wave-

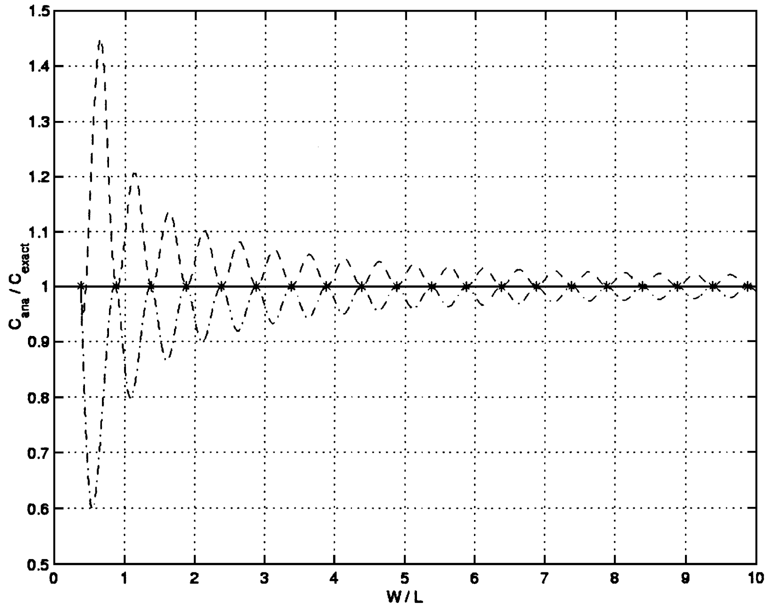

Fig. 20. Analytically determined phase speed by cross-correlation method, for a sine wave signal (- -) and for a cosine wave signal (-·). Analytic least squares phase speed (—) for both signals. Analytically determined window sizes (∗) for $n=0$, $n=1,\ldots$, $n=19$ from Eq. (63).

length. At a window size of twice the wavelength, the error in the cross-correlation estimate is more than 50%, with the error decreasing as the window size increases. Theoretically, the window size can be arbitrarily made as small as desired. It might seem that this would improve spatial resolution, but the errors due to end effects arising from the truncation of the waveform increase with decreasing window size. On the other hand, increasing W leads to a loss in resolution. Using window sizes given by Eq. (63), which are marked by the * in the figure, the exact result is recovered for both waveforms. It is seen that the phase speed for the cosine waveform is always under-predicted, and for the sine waveform always over-predicted. It is therefore difficult to accurately estimate phase speeds for regular wave conditions, using cross-correlation functions. For the same two waveforms, we also calculated the phase speeds numerically using cross-correlations. The estimates are shown in Fig. 21 and agree with the analytic results in Fig. 20.

A.2. Least-squares estimation

Researchers in the field of fracture mechanics have shown that a least-squares optimization procedure removes the drawbacks associated with estimating displacements and flow velocities using cross-correlation functions (McNeil et al., 1987). Following their approach, we develop a least-squares method to avoid the pitfalls associated with small window sizes mentioned in the previous method. We use finite windows as before to sub-sample the given profiles.

The least-squares error at a spatial lag ξ is defined as

$$\varepsilon(\xi) = \int_0^{W-\xi} \{f(x) - g(x+\xi)\}^2 \mathrm{d}x \tag{64}$$

The spatial lag at which this error becomes a minimum can be defined as $\xi_{\min}$, which is obtained from

$$\left.\frac{\mathrm{d}\epsilon(\xi)}{\mathrm{d}\xi}\right|_{\xi=\xi_{\min}} = 0 \tag{65}$$

The phase speed estimate is then given by

$$C = \frac{\xi_{\min}}{\delta t} \tag{66}$$

Fig. 22(a) shows the one-dimensional wave signals considered before for the cross-correlation case, with

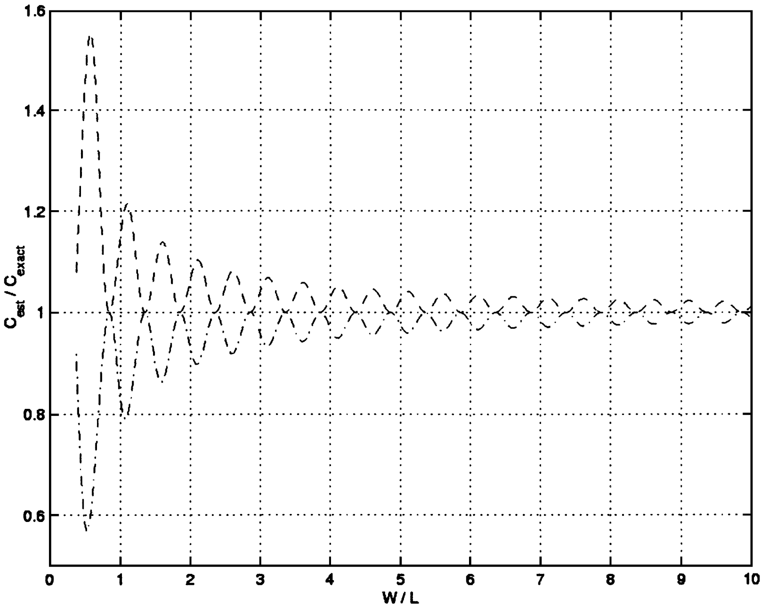

Fig. 21. Numerically estimated phase speed by cross-correlation method, for a sine wave signal (- -) and for a cosine wave signal (-·).

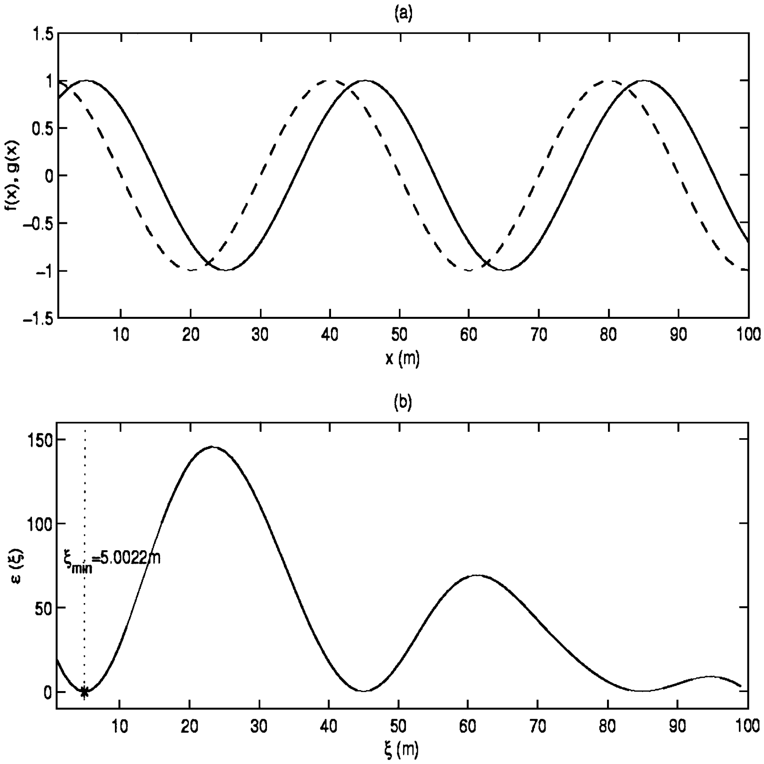

Fig. 22. (a) Spatial maps of surface elevation separated in time. (b) Least squares error between the two profiles as a function of spatial lag.

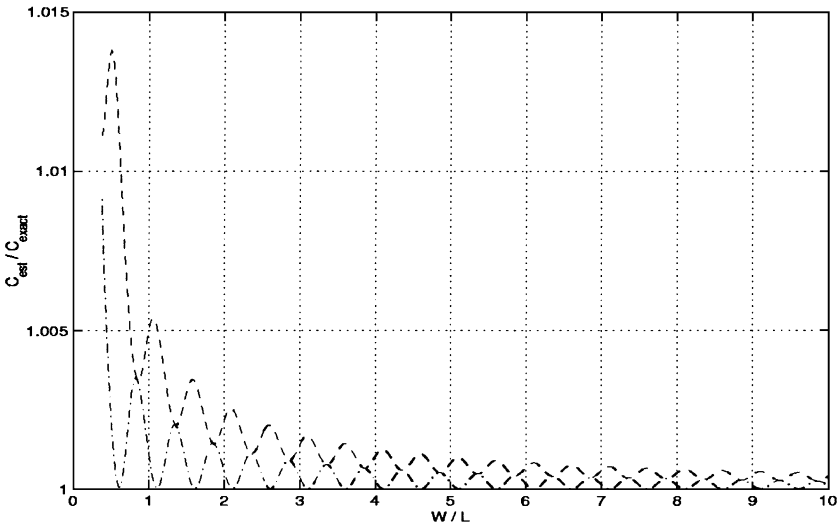

Fig. 23. Effect of window size on estimation of phase speed by least squares method, for a sine wave signal (- -), and for a cosine wave signal (-·).

all parameters remaining the same. The bottom panel shows the least-square error plotted against the spatial lags. The error can be seen to trail off as the lags increase, since less and less of the two waveforms is available for comparison. The first minimum in the error vector is marked as a * in the plot, which occurs at a lag $\xi_{min} = 5.0022$ m. ξ_{min} has been determined to sub-grid accuracy by an analytic three-point parabolic interpolation around the minimum. Since the time-lag between the two signals (δt) is 1 s, the phase speed calculated from Eq. (62) is 5.0022 m/s.

The effect of window size on celerity calculations using least squares has been investigated. On substituting the definition of ξ_{min} from Eq. (66), Eq. (65) is identically satisfied irrespective of window size. The analytic least-squares (the solid line in Fig. 20) value recovers the exact phase speed, since the least-squares error at the minimum lag is zero. The numerically estimated phase speeds (nondimensionalized by the exact value) are plotted against the nondimensionalized window size, for the sine waveform and the cosine waveform in Fig. 23. The mismatch in the estimated and exact phase speed is only due to digitization errors. The error can be observed to decrease as W increases, with the error at a window size equal to the wavelength, being about 0.5%, which is two orders of magnitude smaller than for the cross-correlation case.

References

Beji, S., Battjes, J.A., 1993. Experimental investigations of wave propagation over a bar. Coastal Engineering 19, 151–162.

Bell, P.S., 1999. Shallow water bathymetry derived from an analysis of X-band marine radar images of waves. Coastal Engineering 37, 513–527.

Chen, Q., Kirby, J.T., Dalrymple, R.A., Kennedy, A.B., Chawla, A., 2000. Boussinesq modeling of wave transformation, breaking and runup: II. Two horizontal dimensions. Journal of Waterway, Port, Coastal, and Ocean Engineering 126, 48–56.

Dalrymple, R.A., Kennedy, A.B., Kirby, J.T., Chen, Q., 1998. Determining bathymetry from remotely sensed images. Proceedings 26th International Conference on Coastal Engineering. ASCE, Copenhagen, pp. 2395–2408.

Dugan, J.P., Suzukawa, H.H., Forsyth, C.P., Farber, M.S., 1996. Ocean wave dispersion surface measured with airborne IR imaging system. Proc. 1995 International Geoscience and Remote Sensing Symposium (IGARSS'95). Florence, Italy, pp. 1282–1283.

Gobbi, M.F., Kirby, J.T., 1999. Wave evolution over submerged sills: tests of a high-order Boussinesq model. Coastal Engineering 37, 57–96.

Grilli, S.T., 1998. Depth inversion in shallow water based on nonlinear properties of shoaling periodic waves. Coastal Engineering 35, 185–209.

Hessner, K., Reichert, K., Dittmer, J., 1999a. Coastal application of a wave monitoring system based on a nautical radar. Proc. 1999 International Geoscience and Remote Sensing Symposium (IGARSS'99), Hamburg.

Hessner, K., Reichert, K., Rosenthal, W., 1999b. Mapping of sea bottom topography in shallow seas by using a nautical radar. 2nd International Symposium on Operationalization of Remote Sensing.

Holland, K.T., 2001. Application of the linear dispersion relation with respect to depth inversion using remotely sensed imagery. IEEE Transactions on Geoscience and Remote Sensing 39 (9), 2060–2072.

Keane, R.D., Adrian, R.J., 1992. Theory of cross-correlation analysis of piv images. Applied Science Research 49, 191.

Kennedy, A.B., Chen, Q., Kirby, J.T., Dalrymple, R.A., 2000a. Boussinesq modeling of wave transformation, breaking and run-up: I. One dimension. Journal of Waterway, Port, Coastal, and Ocean Engineering 126, 39–47.

Kennedy, A.B., Dalrymple, R.A., Kirby, J.T., Chen, Q., 2000b. Depth inversion using direct Boussinesq modeling. Journal of Waterway, Port, Coastal, and Ocean Engineering 4, 206–214.

Kinoshita, R., 1967. An analysis of the movement of flood waters by aerial photography, concerning characteristics of turbulence and surface flow. Photographic Surveying 6, 1–17 (in Japanese).

McNeil, S.R., Peters, W.H., Sutton, M.A., 1987. Estimation of stress intensity factor by digital image correlation. Engineering Fracture Mechanics 28 (1), 101–112.

Reichert, K., Hessner, K., Borge, J.C.N., Dittmer, J., 1999. Wamos II: a radar based wave and current monitoring system. Proc. 1999 International Society of Offshore and Polar Engineers (ISO PE'99), Brest, vol. 3, pp. 1–5.

Roesgen, T., Totaro, R., 1995. Two-dimensional on-line particle imaging velocimetry. Experiments in Fluids 19, 188–193.

Stockdon, H.F., Holman, R.A., 2000. Estimation of wave phase speed and nearshore bathymetry from video imagery. Journal of Geophysical Research 105, 22015–22033.

Utami, T., Blackwelder, R.F., Ueno, T., 1991. A cross-correlation technique for velocity field extraction from particulate visualization. Experiments in Fluids 10, 213–223.

Wei, G., Kirby, J.T., Grilli, S.T., Subramanya, S., 1995. A fully nonlinear Boussinesq model for surface waves. I. Highly nonlinear unsteady waves. Journal of Fluid Mechanics 294, 71–92.

Willert, C.E., Gharib, M., 1991. Digital particle image velocimetry. Experiments in Fluids 10, 181–193.

Williams, J.Z., Piotrowski, C.C., Dugan, J.P., Campion, D.C., 2000. Airborne optical measurements for estimating directional wave spectra, currents and water depth. 6th International Workshop on Wave Hindcasting and Forecasting, Monterey, California.